学位論文

Decomposition of trapped cyclohexane ions in intense laser fields
and development of an ion beam apparatus

(強光子場中のシクロヘキサンイオンの分解反応

及びイオンビーム装置の開発)

平成 28 年 7 月　博士　（理学）申請

東京大学大学院理学系研究科

化学専攻

山崎　嵩雄

Abstract

The present thesis starts with the general introduction, in which the previous and recent experimental studies on responses of mass selected molecular ions to an intense laser field are introduced, and the available experimental techniques for separating specific molecular ion species for investigating crucial steps in the interaction between molecules and an intense laser field are described.

In Chapter 2, the experimental study on decomposition of cyclohexane parent ions by the irradiation with an ultrashort near-infrared laser pulse is described. By the technique of ion-trap time-of-flight mass spectrometry, cyclohexane parent ions were stored mass-selectively in an ion trap, and decomposed by the irradiation of intense ultrafast laser pulses. From the laser-field intensity dependences of the yields of the fragment ions, the numbers of photons required for the generation of the respective fragment ion species were estimated.

In Chapter 3, a mass-selective ion beam source for coincidence measurements were developed. The apparatus was composed of a duoplasmatron ion source, a quadrupole mass filter, a quadrupole deflector, an interaction zone composed of stacked electrodes, and a fragment detector. The characterization of the mass-selected CO_2^+ ion beam was achieved by monitoring the beam profiles by the fragment detector. From the observed ion beam size, the ion density of the ion beam was calculated and signal count rate was estimated.

Finally, in Chapter 4, the contents of the present thesis are summarized.

Table of contents

Chapter 1. General Introduction

When neutral molecules are irradiated with femtosecond intense laser pulses whose electric field intensity is as high as 10^{14} W/cm^2, these molecules are in most cases ionized immediately at the rising edge of the laser pulses, and the interaction between the generated molecular ions and the intense laser field induces a variety of subsequent phenomena such as electronic excitation, multiple ionization, Coulomb explosion, skeletal structural deformation, and hydrogen migration (Fig. 1-1). Because molecules are cations during the major part of the interaction period with the light field, it should be meaningful to investigate experimentally the interaction of molecules with such an intense laser field starting from molecular ion species.

In general, experiments on photodecomposition of ion species are difficult mainly because the sample density of ion species is inevitably extremely low. Under typical experimental conditions, the sample density is as low as around 10^7 cm^{-3} or even lower, corresponding to 10^{-7} Pa or lower, which is comparable with the number density of a background gas under standard high-vacuum conditions of gas phase beam experiments. Consequently, the number of experimental reports on decomposition processes of molecular ions in an intense laser field is much fewer than those of experiments starting from neutral molecules.

There are several of pioneering studies in which molecular ions are exclusively irradiated with an ultrashort intense laser pulses. For example, I may raise the report made by Gerber and coworkers on the laser-field intensity dependences of the Coulomb explosion pathways of sodium dimer ions, Na_2^+ [1]. In their experiment, Na_2^+ ions were generated by resonantly enhanced multiphoton ionization (REMPI) with nanosecond laser pulses, and the generated ions were drifted upward, and then, irradiated with femtosecond intense laser pulses.
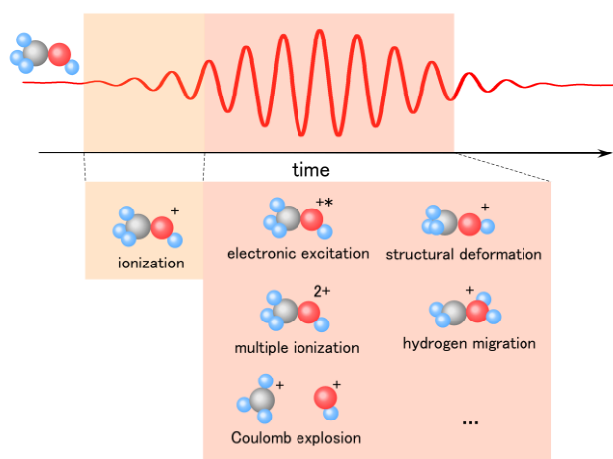
Fig. 1-1.   Schematic of molecular dynamics in intense laser fields.

In most of the previous studies, the molecular ions investigated were mostly diatomic and triatomic molecular ions, as reviewed by Ben-Itzhak [2]. Indeed, intense-field photodissociation experiments for larger molecular ions containing more than three atoms have been limited to a series of experiments on aromatic molecular ions [3-5] and their clusters [4, 6, 7] by tandem time-of-flight mass spectrometry performed by our group at the University of Tokyo, and to ion trap experiments on peptide ions studied by Reid and coworkers [8-10].

Our group investigated dynamics of benzene ion by tandem time-of-flight mass spectrometry. In the series of experiments, benzene (C_6H_6) [3], aniline ($C_6H_5NH_2$) [4], and van der Waals complexes formed between aniline and ammonia, $C_6H_5NH_2$--$(NH_3)_n$ [7] were ionized by REMPI, and specific ion species were selected by the first stage of the mass separation achieved by time-of-flight. Then, the ion species having the specific mass were irradiated with femtosecond intense laser pulses, and the fragment ion species were analyzed by the second time-of-flight stage. For benzene, Itakura and co-workers [3] observed a significant wavelength dependence in the ionization and decomposition processes of benzene cation, $C_6H_6^+$, in an intense laser field. They found that, with 800 nm laser pulses, benzene cations $C_6H_6^+$ are further ionized efficiently into benzene dications $C_6H_6^{2+}$ whereas, with 400 nm laser pulses, benzene cations are decomposed into fragment ions.

In Chapter 2 of the present thesis, in order to increase the number density of sample ion species, we introduced an ion trap apparatus, and investigated the decomposition processes of cyclohexane ion, trapped and accumulated in the ion trap, in intense femtosecond laser fields by ion trap mass spectrometry [11]. From the precise analyses of the laser field intensity dependences of the yields of the fragment ions, the mechanism of the decomposition processes of cyclohexane have been explored.

On the other hand, as long as only charged fragment ions are detected, we could not securely specify dissociation pathways of such mass selected cation molecules in which one or more neutral fragments produced. One of the promising approaches is to accelerate the parent mass selected cation molecules to more than 10^3 eV so that even neutral fragments can be detected by a microchannel plate detector [12-14]. In Chapter 3 of this thesis, the development of an ion beam source, which was designed and constructed for investigating many body decomposition processes of cation molecular species after their interaction with an intense laser pulse, is described.

Chapter 2. Decomposition of cyclohexane ion induced by intense femtosecond laser fields by ion-trap time-of-flight mass spectrometry

2.1. Introduction

When neutral molecules are ionized by intense femtosecond laser pulses in the near-infrared region, decomposition into smaller sized fragment ion species is largely suppressed when compared with picosecond and nanosecond laser ionization, and parent ions are observed as a main ion product [15-20]. Therefore, ionization with femtosecond near-infrared intense laser pulses yielding simple mass spectra has an advantage in the analysis of chemical species in gaseous samples. However, some molecular species exhibit significant fragmentation even when they are ionized with near-infrared femtosecond laser pulses [21-24]. Fuß *et al.* [25] reported a drastic difference in mass spectra of ionization of the two neutral isomers having the same chemical formula of C_6H_8, i.e., the parent ion species dominate in the mass spectra of 1,3-cyclohexadiene while a variety of small fragment ion species show up in the mass spectra of 1,3,5-hexatriene. This significant fragmentation in the ionization of 1,3,5-hexatriene was ascribed to the efficient photoabsorption of 1,3,5-hexatriene cation, $C_6H_8^+$, through the resonance electronic transition at the laser wavelength of 800 nm.

More directly, our group reported the wavelength effect in the fragmentation of benzene cation by tandem time-of-flight mass spectrometry [3], in which mass-selected benzene parent ions $C_6H_6^+$ were initially prepared and were irradiated with femtosecond laser pulses at 400 nm and 800 nm, and showed that benzene parent ions were found to be decomposed into the fragment ions at 400 nm while doubly-charged benzene ions were generated at 800 nm. This significant wavelength dependence was attributed to the electronic resonance at 400 nm in benzene cation $C_6H_6^+$.

Harada *et al.*[26] recorded mass spectra of two pairs of neutral isomers, i.e., "2,3-dimethyl-1,3-butadiene and 2,5-dimethy-2,4-hexadiene," and "1,4-cyclohexadiene and 1,3-cyclohexadiene" after the irradiation of 800 nm femtosecond laser pulses, and found that significant fragmentation proceeds when parent cations have an absorption band at around 800 nm. Nakashima and coworkers [27-29] recorded mass spectra of some other organic compounds by irradiating them with femtosecond laser pulses at various wavelengths in the near-infrared region, and confirmed a tendency that significant fragmentation proceeds when the absorption band of cations exists at the wavelength of the excitation laser pulses.

On the other hand, except for our study on benzene cations [3], no report has been made on the fragmentation enhancement by a resonance electronic transition of organic molecular ions separated spatially from neutral parent molecules. Therefore, the measurements of the photofragmentation processes of organic compound starting from their cations have been awaited for more detailed discussion on the mechanism of the fragmentation enhancement.

In general, experiments on photodecomposition of ion species are difficult because their sample density is inevitably extremely low. Under typical experimental conditions, the sample density is around 10^7 cm^{-3} or lower, corresponding to 10^{-7} Pa or lower, and is the same as the number density of a background gas under standard high-vacuum conditions of gas-phase beam experiments.

5

Consequently, the number of experimental reports on decomposition processes of molecular ions in intense laser fields is much fewer than those of experiments starting from neutral molecules.   In the previous studies of photodissociation processes of molecular ions, the molecular ions were mostly diatomic and triatomic molecular ions, as reviewed by Ben-Itzhak [2].   Indeed, intense-field photodissociation experiments for larger molecular ions containing more than three atoms have been limited to a series of our experiments on aromatic molecular ions [3-5] and their clusters [4, 6, 7] by tandem time-of-flight mass spectrometry, and to ion trap experiments on peptide ions studied by Reid and coworkers [8-10].

In the present study, we developed an ion-trap time-of-flight mass-spectrometry apparatus in order to investigate photodecomposition of mass-selected molecular ions in femtosecond intense laser fields by modifying our previously built apparatus that was used for the measurements of photofragment excitation spectra of aniline cation with tunable nanosecond laser pulses [30].   By using the newly developed ion-trap time-of-flight mass-spectrometry apparatus, we have investigated photodecomposition processes of cyclohexane cation in femtosecond laser fields at the wavelength of 800 nm.   Cyclohexane, chosen in the present study as a sample gas, is known to exhibit significant photofragmentation by the irradiation of femtosecond intense 800 nm laser pulses onto neutral cyclohexane [21-23, 28, 31-33], and this efficient fragmentation was previously ascribed to the resonance electronic transition of cyclohexane cation at 800 nm [34-36].   In order to clarify the fragmentation mechanisms, we have investigated the laser-field intensity dependence of the decomposition processes of cyclohexane cations stored in the ion trap by irradiating them with intense femtosecond laser pulses at 800 nm at the different laser field intensities in the wide range of $5.7 \times 10^{11} \sim 8.0 \times 10^{13}$ W/cm^2.

2.2. Experimental

Figure 2-1(a) shows the schematic of the experimental setup. The apparatus is composed of a molecular beam source, a Paul-type ion trap, and a time-of-flight (TOF) mass spectrometer. Neutral cyclohexane molecules (99.0%, Wako Pure Chemical Industries, Ltd., JPN) were introduced into a vacuum chamber through a pulsed nozzle operated at the repetition rate of 5 Hz for 30 ms, and the pulsed molecular beam was collimated using a skimmer whose orifice diameter is 0.5 mm to form a pulsed effusive molecular beam. After neutral cyclohexane molecules were introduced into the central area of the ion trap, they were ionized by femtosecond laser pulses ($\lambda = 800$ nm, $\Delta\tau = 40$ fs, $I = 6.3\times10^{13}$ W/cm^2) at the repetition rate of 5 kHz. The generated cyclohexane parent ions $C_6H_{12}^+$ were trapped exclusively by adjusting the radiofrequency (RF) voltages applied to the central ring electrode of the ion trap at the RF frequency of 500 kHz.

The timing chart of the experiment is shown in Fig. 2-1(b). After repeating the photoionization and the mass-selective ion trapping of $C_6H_{12}^+$ around 150 times during the entire period of the sample injection (30 ms) to accumulate and store $C_6H_{12}^+$ molecules exclusively in the ion trap, the ionization laser pulses were blocked by a mechanical beam shutter (S1 in Fig. 2-1(c)). The accumulated $C_6H_{12}^+$ ions were kept stored in the ion trap for the next 70 ms in order to decrease the number of neutral C_6H_{12} molecules, remaining in the ion trap, through the diffusion process. Then, the RF voltage for the trapping was switched off, and the stored $C_6H_{12}^+$ ions were irradiated with a femtosecond laser pulse ($\lambda = 800$ nm, $\Delta\tau = 40$ fs) to induce photofragmentation by opening another mechanical shutter (S2 in Fig. 2-1(c)). The intensity of the laser pulses for the photofragmentation was varied in the wide intensity range between 5.7×10^{11} and 8.0×10^{13} W/cm^2. Because of an inevitable timing jitter with ±1 μs of the switch-off time of the RF voltage whose frequency is 500 kHz, referred hereafter to the RF-off time, the time-delay between the RF-off time and the laser irradiation for the photofragmentation was adjusted so that it falls in the range between 0.2 and 2.2 μs. The generated fragment ions were extracted from the ion trap by applying a pulsed high-voltage to the end-cap electrodes of the ion trap, and were recorded by TOF mass spectrometry. The present TOF measurements were performed by applying the pulsed high voltage after the irradiation of the fragmentation laser pulses, in which the delay time of the extraction voltage was not adjusted to the time-lag energy focusing conditions [37]. Therefore, it is difficult to discuss quantitatively the released kinetic energies in the fragmentation processes from the peak profiles in the TOF spectra. Because the signals of the fragment ions were extremely weak, the TOF mass spectral data recorded at each ion-extraction step were transferred into a personal computer (PC) and analyzed by the ion counting scheme to raise the signal-to-noise ratio of the mass spectra. After the TOF mass spectrum is recorded, the S2 was closed in order to block the fragmentation laser pulses. Then, the ionization pulses were introduced by opening the S1. This sequence was repeated at the repetition rate of 5 Hz.
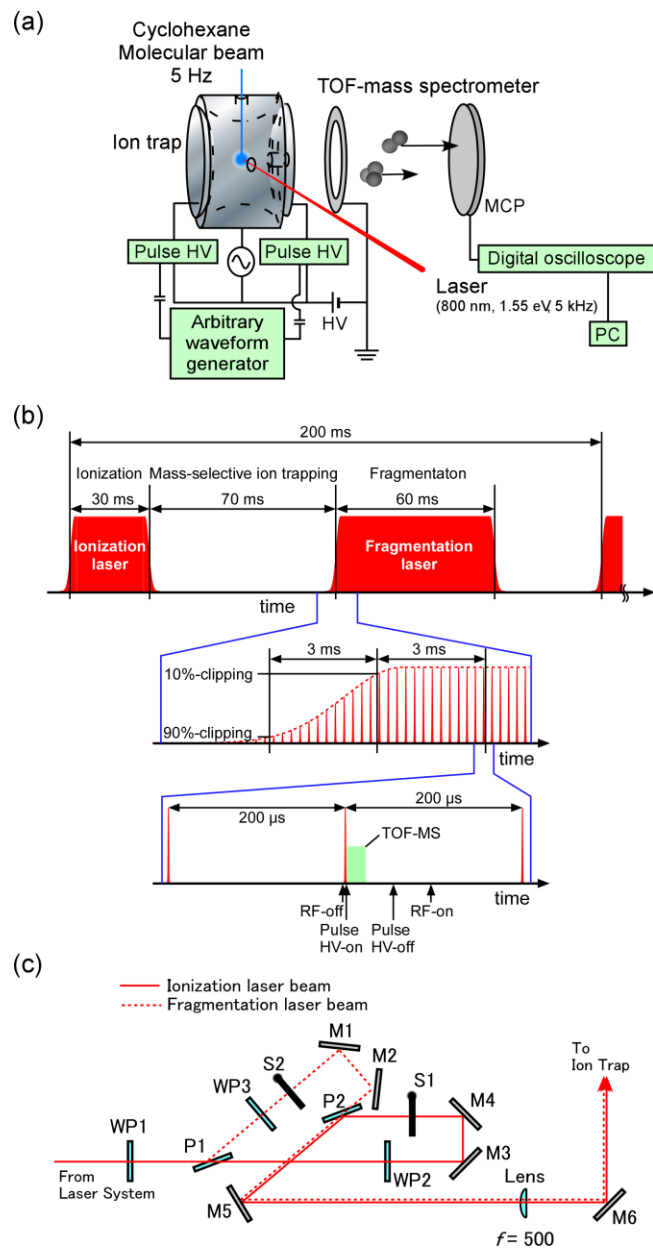
Fig. 2-1.　Schematics of the experimental setup: (a) an apparatus for ion-trap time-of-flight mass spectrometry, (b) a timing chart, and (c) an optical layout for the present measurements.

It is difficult to discuss quantitatively the vibrational state distribution of trapped cyclohexane ions just before the irradiation of the fragmentation pulses. However, because the period (70 ms) of mass-selective trapping of cyclohexane ions is longer than or comparable to the typical radiative decay lifetimes of IR active vibrational modes, $10^0 \sim 10^2$ ms, the degree of vibrational excitation of the trapped cyclohexane is considered to be lower than that just after the ionization to a certain extent.

Because the signals of the fragment ions generated through the dissociative ionization of neutral C_6H_{12} remaining in the ion trap yields the background signals of the fragment ions originating from the trapped $C_6H_{12}^+$, the background mass spectra were recorded separately, and were subtracted from the mass spectra that were recorded with $C_6H_{12}^+$ ions stored in the ion trap. In order to record the background signals, we adopted a method called stored waveform inverse Fourier transform (SWIFT) [38], by which the trapped ions are expelled from the ion trap by applying RF voltage outputs of an arbitrary function generator to the two endcap electrodes of the ion trap via coupling capacitors, and expelled all of the stored $C_6H_{12}^+$ ions from the ion trap before introducing a laser pulse to induce the fragmentation.

The optical layout of the present measurements is shown in Fig. 2-1(c). The output of Ti:Sapphire laser system (5 kHz, 40 fs, 0.5 mJ/pulse) was split into two beams by a half wave plate (HWP1) and a thin film polarizer (P1). The pulse energies of the two laser beams were independently adjusted by half wave plates (HWP2, HWP3) locating at each beam line, and the two beams were recombined by another thin film polarizer (P2). One of the laser beams was used for the ionization of neutral C_6H_{12} molecules, and the other was for the fragmentation of parent molecular ions $C_6H_{12}^+$ stored in the ion trap. The polarization vector of the ionization laser pulses was set to be perpendicular to the TOF axis, while the polarization vector of the fragmentation laser pulses was set to be parallel to the TOF axis. Both of the ionization and fragmentation laser pulses were focused onto the central area of the ion trap with an f = 500 mm plano-convex lens. The beam profile at the focal spot was measured by a beam profiler, and it was confirmed to be a clean Gaussian and that the beam waist diameter was 145 μm.

The mechanical shutters (S1, S2) were installed in both of the beam lines for on-off control of the laser pulses. Because the response time of the shutters was longer than the pulse-to-pulse separation (200 μs) of the 5 kHz laser system, the laser beam profiles were partially clipped during the shutter motion. It took around 3 ms for the on-off motion of the shutters between the shutter position for clipping 90% of the laser beam profile and that for clipping 10% of the laser beam profile, as shown Fig. 2-1(b). In order not to collect fragment ions generated by those clipped laser pulses, the pulsed high voltage for the extraction of fragment ions was applied ~3 ms after the timing of 10%-clipping. Because no fragment ion signals were detected in the TOF spectra when the pulsed extraction voltage was applied ~190 μs after the irradiation of the fragmentation laser pulse, it was

confirmed that fragment ions generated by the prior fragmentation laser pulse were expelled almost completely from the ion trap during the pulse-to-pulse period (200 μs). It is possible that a trace amount of neutral fragments generated by the preceding laser pulse could survive in the ion trap for more than 200 μs, but, even when they exist, their contribution is eliminated by the subtraction of the background mass spectra.

Because the number density of the trapped ions was very low ($\sim 10^6$ cm^{-3}) in the present study, the suppression of the number density of neutral cyclohexane molecules in the ion trap was crucial. In order to suppress ion signals originating from the dissociative photoionization of background neutral C_6H_{12}, the electrodes of the ion trap were cooled down to about 77 K with liquid nitrogen in order to reduce the number density of neutral C_6H_{12} by the cryogenic-pump effect, and the background pressure of the vacuum chamber was kept to be around 3×10^{-7} Pa during the measurements.

2.3. Results and discussion

A. Laser-field intensity dependences of fragment ion yields

The mass spectrum of ion species generated by ionization of neutral cyclohexane molecules with femtosecond intense laser pulses (800 nm, 40 fs, 2.1×10^{14} W/cm^2) is shown in Fig. 2-2. Various kinds of ion species, such as $C_6H_{11}^+$, $C_5H_n^+$ ($n = 7 \sim 11$), $C_4H_n^+$ ($n = 5 \sim 8$), $C_3H_n^+$ ($n = 3 \sim 7$), $C_2H_n^+$ ($n = 2 \sim 6$), and CH_3^+ were detected as the product fragment ions generated through the dissociative ionization of neutral C_6H_{12}. The overall feature of the observed mass spectrum is consistent with those reported by the previous studies [21-23, 28, 31-33]. It should be noted that the fragment ions such as $C_5H_{11}^+$, $C_3H_7^+$, $C_2H_6^+$, $C_2H_5^+$, and CH_3^+ can only be generated after hydrogen migration processes. The hydrogen migration processes induced by an intense laser field have been observed in a wide variety of hydrocarbon molecular species in intense laser fields [39].

In order to investigate decomposition processes from $C_6H_{12}^+$, only $C_6H_{12}^+$ ions need to be stored before the irradiation of an intense laser pulse inducing their decomposition. The mass spectrum in Fig. 2-3 shows that the mass-selective accumulation of $C_6H_{12}^+$ ($m/z = 84$) was achieved almost completely before the irradiation of the laser pulse for the decomposition of $C_6H_{12}^+$. However, when the mass spectrum around the peak of $C_6H_{12}^+$ ($m/z = 84$) is expanded (red solid line in the inset of Fig. 2-3), small peaks of $^{12}C_6H_{11}^+$ and $^{13}C^{12}C_5H_{12}^+$ can be recognized at the left and right sides of the peak of $C_6H_{12}^+$, respectively. The yield ratio of $^{12}C_6H_{11}^+$ relative to the main peak is around 10%, and the yield ratio of $^{13}C^{12}C_5H_{12}^+$ relative to the main peak is about 6%, which is consistent with the ratio (6.4%) estimated from the natural abundance ratio of ^{13}C.
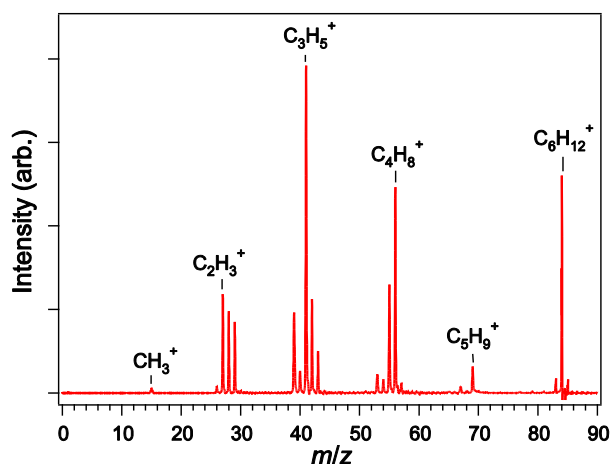
Fig. 2-2. Mass spectrum of ion species generated by the ionization of neutral cyclohexane molecules with femtosecond intense laser pulses (800 nm, 40 fs, 2.1×10^{14} W/cm^2).

11
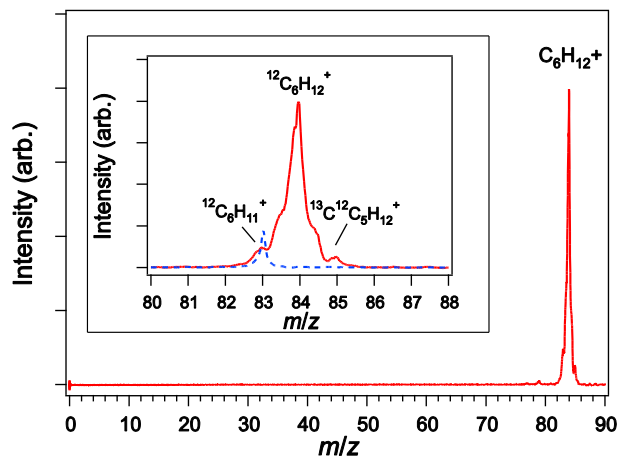
Fig. 2-3. Mass spectrum of the trapped ions after the mass-selective ion accumulation for cyclohexane parent ions. Inset: The expanded view around the peak of $C_6H_{12}^+$ (red solid curve). Mass spectrum of the trapped ions after the mass-selective ion accumulation for $C_6H_{11}^+$ (blue broken line).

Figure 2-4(a) shows a mass spectrum of fragment ions generated from the stored $C_6H_{12}^+$ by the irradiation of a femtosecond laser pulse at the laser field intensity of 8.0×10^{13} W/cm^2. Various fragment ion species, such as $C_5H_n^+$ (n = 7, 9), $C_4H_n^+$ (n = 5~8), $C_3H_n^+$ (n = 3~7), $C_2H_n^+$ (n = 2~6), and CH_3^+, were identified in the recorded mass spectrum, showing that the photodecomposition reactions proceed efficiently by the absorption of 800 nm light. Figure 4(b) shows a mass spectrum of the fragment ions obtained when the laser field intensity was lowered to 5.7×10^{11} W/cm^2. At this weaker field intensity, the signal of $C_4H_8^+$ (m/z = 56) is dominant and the relative signal intensities of the smaller fragment ions such as $C_3H_n^+$ (n = 3, 5) and $C_2H_n^+$ (n = 3~5) become much smaller than in Fig. 2-4(a), suggesting that absorption of a larger number of photons is necessary for generating the smaller fragment ions. In Fig. 2-4(a), the peak intensity of m/z = 57 is ~3.8% with respect to that of m/z = 56 ($C_4H_8^+$). Therefore, it is highly probable that the main origin of the peak at m/z = 57 is $^{13}C^{12}C_3H_8^+$, whose relative abundance is calculated to be 4.3%. Similarly, the peak intensity of m/z = 44 is ~3.6% with respect to that of m/z = 43 ($C_3H_7^+$) as shown in the inset of Fig. 2-4(a), and thus, the main origin of the peak at m/z = 44 should be $^{13}C^{12}C_2H_7^+$, whose relative abundance is 3.2%.
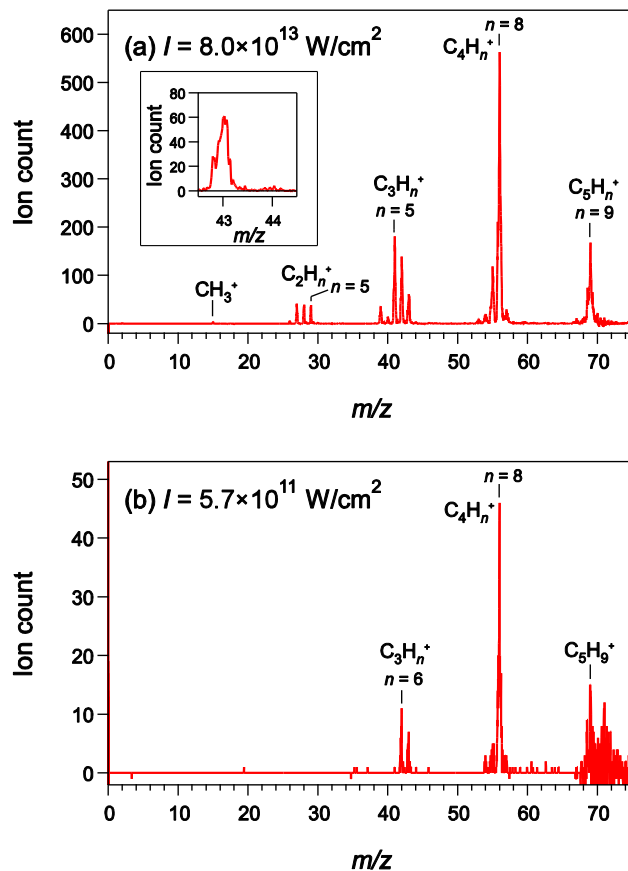
Fig. 2-4. Mass spectra of the fragment ions generated through the photodecomposition of the stored $C_6H_{12}^+$ obtained by the irradiation of femtosecond laser pulses: (a) $I = 8.0 \times 10^{13}$ W/cm²; Inset: The expanded view of $m/z = 43$ and 44. (b) $I = 5.7 \times 10^{11}$ W/cm².

A broken line in the inset of Fig. 2-3 is a mass spectrum of trapped ions when the ion trap conditions were adjusted for trapping only $^{12}C_6H_{11}^+$ ($m/z = 83$) with higher mass selectivity. This mass spectrum shows that the $^{12}C_6H_{11}^+$ were exclusively stored and that, from the comparison with the red solid line of the inset of Fig. 2-3, the number of the trapped $^{12}C_6H_{11}^+$ under these trapping conditions for $^{12}C_6H_{11}^+$ is comparable to the number of trapped $^{12}C_6H_{11}^+$ under the trapping conditions for $^{12}C_6H_{12}^+$. When the trapped ions stored under the trapping conditions for $^{12}C_6H_{11}^+$ was irradiated with the fragmentation laser pulse, no fragment ions were detected even at the laser field intensity of the fragmentation laser pulse was 1.0×10^{14} W/cm². This result clearly shows that fragment ion signals originating from $^{12}C_6H_{11}^+$ are negligibly small in Figs. 2-4(a) and (b), which were recorded at the laser field intensities of 8.0×10^{13} W/cm² and 5.7×10^{11} W/cm², respectively. This small dissociation probability of $^{12}C_6H_{11}^+$ suggests that $^{12}C_6H_{11}^+$ could not be excited resonantly to its electronic excited states by 800 nm light [26].

13

According to the photoelectron spectroscopy of cyclohexane [40], the energy difference between the photoelectron peak corresponding to the electronic ground D_0 E_g state of cyclohexane cation whose configuration is $(4e_g)^{-1}$, i.e., $(core)^{24}(3a_{1g})^2(3a_{2u})^2(3e_g)^4(3e_u)^4(1a_{1u})^2(4e_u)^4(4a_{1g})^2(4e_g)^3$, and that corresponding to the second electronically excited D_2 E_u state whose configuration is $(4e_u)^{-1}$ is ~1.67 eV, where the notation of the electronic configurations is based on D_{3d} point group symmetry by assuming that cyclohexane cation takes the chair conformation. The energy levels of cyclohexane cation are schematically shown in Fig. 2-5. Because the photon energy of 800 nm light is 1.55 eV, the one-photon resonance can be achieved for the transition to the D_2 E_u $(4e_u)^{-1}$ state. There is no *gerade* electronic state around the energy range corresponding to the two-photon absorption (3.10 eV), while the fourth excited state (D_4 E_u) having *ungerade* symmetry with the configuration of $(3e_u)^{-1}$ is located at ~3.08 eV. This means that the two-photon absorption to the fourth excited state could become allowed vibronically as long as a vibrational mode having *ungerade* symmetry is excited by odd vibrational quanta. The D_4 E_u state can further be excited to the fifth excited D_5 E_g state lying ~1.3 eV above the D_4 E_u state by another one-photon absorption.
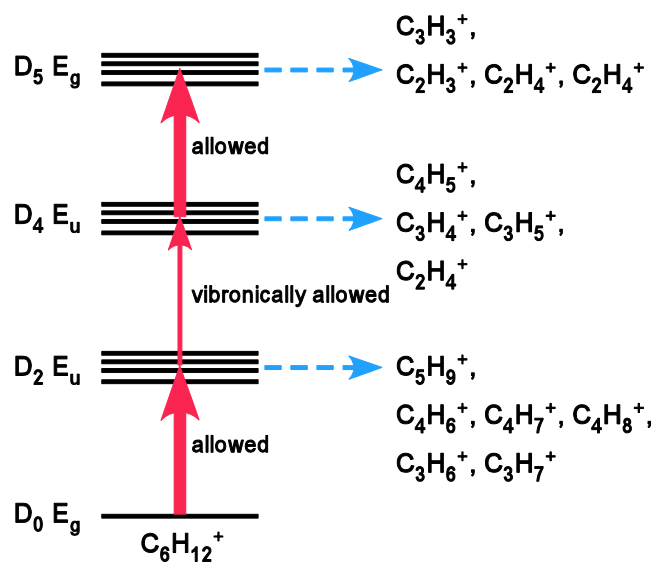
Fig. 2-5. Schematic of the fragmentation pathways induced by the irradiation of femtosecond intense laser pulses onto $C_6H_{12}^+$.

Figures 2-6(a)-(e) show double logarithmic plots of the yields of fragment ion species generated from $C_6H_{12}^+$ as a function of the laser field intensity.　The uncertainties of the data points were estimated from the square root of the ion counts.　The double logarithmic plots for $C_5H_9^+$ (m/z = 69), $^{13}C^{12}C_3H_8^+$ (m/z = 57), and $C_4H_8^+$ (m/z = 56) are shown in Fig. 2-6(a).　Similarly, the double logarithmic plots for $C_4H_7^+$ (m/z = 55), $C_4H_6^+$ (m/z = 54), and $C_4H_5^+$ (m/z = 53) are shown in Fig. 2-6(b), those for $^{13}C^{12}C_2H_7^+$ (m/z = 44), $C_3H_7^+$ (m/z = 43), and $C_3H_6^+$ (m/z = 42) in Fig. 2-6(c), those for $C_3H_5^+$ (m/z = 41), $C_3H_4^+$ (m/z = 40), and $C_3H_3^+$ (m/z = 39) in Fig. 2-6(d), and those for $C_2H_5^+$ (m/z = 29), $C_2H_4^+$ (m/z = 28), and $C_2H_3^+$ (m/z = 27) in Fig. 2-6(e).　The straight lines in Figs. 2-6(a)-(e) show the results of the least-squares fitting assuming that the ion yield (Y) and the laser field intensity (I) can be described as

$$Y = \alpha I^{\beta}, \qquad\qquad\qquad\qquad (2\text{-}1)$$

where α and β are fitting parameters.　In the logarithmic plots in Figs. 2-6(a)-(e), β represents the slopes of the straight lines.　The optimized values for these two parameters are summarized in Table I.

15
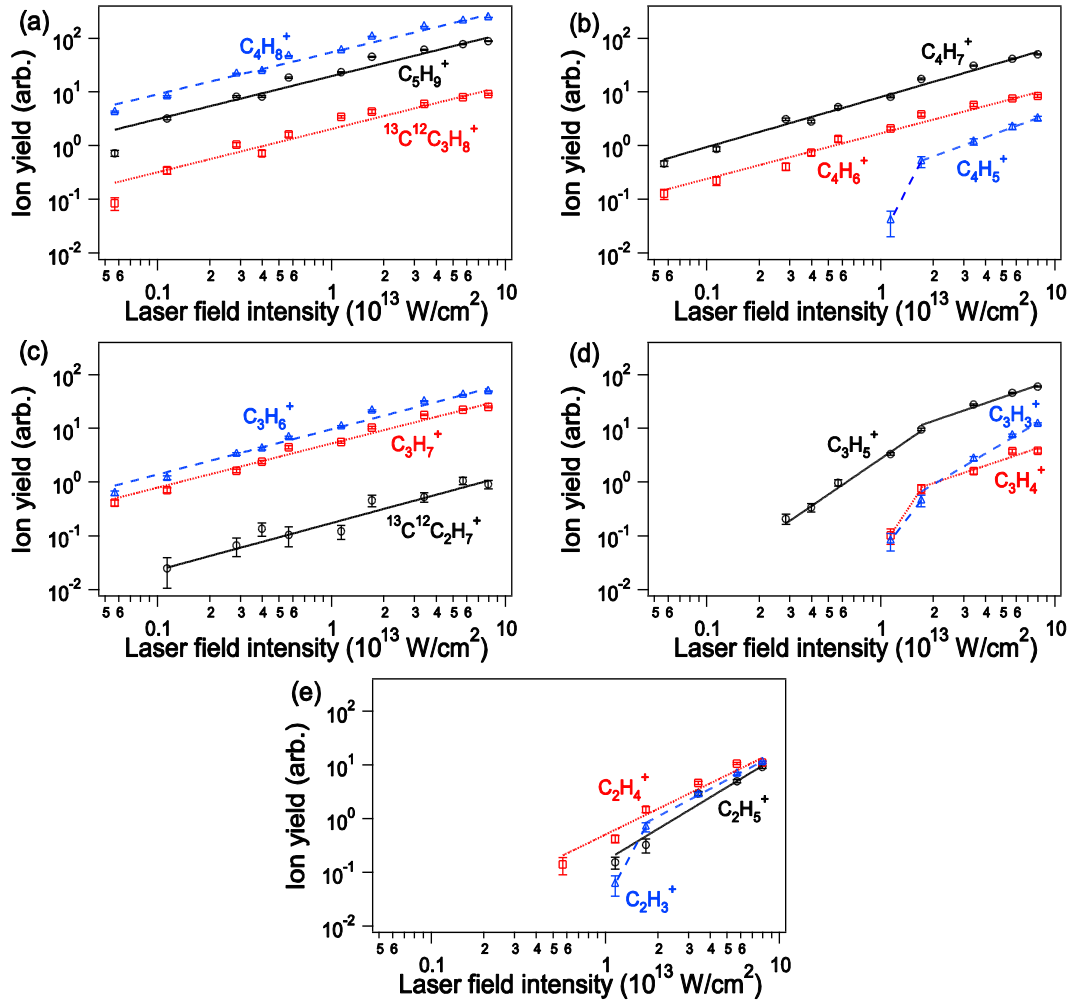
Fig. 2-6. Laser-field intensity dependences of the yields of the fragment ions produced by the irradiation of femtosecond intense laser pulses onto $C_6H_{12}^+$. (a) Black open circle: $C_5H_9^+$; Red open square: $^{13}C^{12}C_3H_8^+$; Blue open triangle: $C_4H_8^+$. (b) Black open circle: $C_4H_7^+$; Red open square: $C_4H_6^+$; Blue open triangle: $C_4H_5^+$. (c) Black open circle: $^{13}C^{12}C_2H_7^+$; Red open square: $C_3H_7^+$; Blue open triangle: $C_3H_6^+$. (d) Black open circle: $C_3H_5^+$; Red open square: $C_3H_4^+$; Blue open triangle: $C_3H_3^+$. (e) Black open circle: $C_2H_5^+$; Red open square: $C_2H_4^+$; Blue open triangle: $C_2H_3^+$.

TABLE I. The α, β, E_{AE}, and E_{th} values for respective fragment ions.

Fragment ion	Mass/ amu	α/ arb.	β	E_{AE}/eV	E_{th}/eV; [Fragmentation channel]
$C_5H_9^+$	69	19.5(2)	0.800(7)	<1.3,[a] 1.27,[b] 0,[c] ≤1.18,[d] $1.19(4)$[f]	0.84; [$CH_3CHCH=CHCH_3^+ + CH_3$]
$C_4H_8^+$	56	54.2(3)	0.780(3)	<1.3,[a] 1.57,[b] $1.27(3)$,[e] $1.20(1)$[f]	0.93; [(E)-2-$C_4H_8^+$ + C_2H_4]
$C_4H_7^+$	55	8.02(12)	0.932(10)	$(>1.3, <3.0)$,[a] $1.33(4)$[f]	1.40; [$C_4H_7^+$ + C_2H_5]
$C_4H_6^+$	54	1.69(5)	0.848(20)		1.62; [$CH_3C{\equiv}CCH_3^+$ + C_2H_6]
$C_4H_5^+$	53	0.274(64)‡	6.24† 1.19(14)‡		2.92; [$CH_3-(cyclo\text{-}C_3H_2)^+$ + C_2H_5 + H_2]
$C_3H_7^+$	43	5.22(10)	0.823(11)	$3.62(8)$,[e] $1.61(3)$[f]	1.37; [$C_3H_7^+$ + C_3H_5]
$C_3H_6^+$	42	9.58(13)	0.843(8)	$(>1.3, <3.0)$,[a] $2.12(7)$,[e] $1.35(4)$[f]	1.57; [$C_3H_6^+$ + C_3H_6]
$C_3H_5^+$	41	2.72(11)† 6.36(31)‡	2.21(9)† 1.11(3)‡	$(>1.3, <3.0)$,[a] $3.32(8)$[e]	2.19; [$C_3H_5^+$ + C_3H_7]
$C_3H_4^+$	40	0.448(84)‡	4.93† 1.09(11)‡		2.00; [$CH_2=C=CH_2^+$ + C_3H_8]
$C_3H_3^+$	39	0.238(38)‡	4.25† 1.92(9)‡		3.53; [$C_3H_3^+$ + C_3H_8 + H]
$C_2H_5^+$	29	0.163(23)	1.96(8)		2.02; [$C_2H_5^+$ + C_4H_7]
$C_2H_4^+$	28	0.502(41)	1.58(5)		2.29; [$C_2H_4^+$ + C_4H_8]
$C_2H_3^+$	27	0.331(53)‡	6.01† 1.71(9)‡		3.42; [$C_2H_3^+$ + C_4H_9]

†Results obtained from data in the intensity range of $I \leq 1.7\times10^{13}$ W/cm^2.
‡Results obtained from the data in the intensity range of $I \geq 1.7\times10^{13}$ W/cm^2.
[a]Charge exchange mass spectrometry [41].
[b]Mass spectrometry with electron impact ionization [42].
[c]Mass spectrometry with electron impact ionization [43].
[d]Mass spectrometry with electron impact ionization [44].
[e]Mass spectrometry with electron impact ionization [45].
[f]Mass spectrometry with photoionization [46].

1. Fragments produced by one-photon absorption

a. $C_5H_9^+$ and $C_4H_n^+$ ($n = 6\sim8$)

Because the β values for $C_5H_9^+$ and $C_4H_n^+$ ($n = 6\sim8$) are around 1.0 or smaller than 1.0, these fragment ions can be regarded as those generated from the $D_2\ E_u$ state of $C_6H_{12}^+$ after the one-photon absorption from the $D_0\ E_g$ state as shown in Fig. 2-5.

b. $C_3H_n^+$ ($n = 6, 7$)

The β values for $C_3H_n^+$ ($n = 6, 7$) are in the range between 0.8 and 0.9, indicating that these ion species were produced from the $D_2\ E_u$ state of $C_6H_{12}^+$ after the one-photon absorption as shown in Fig. 2-5.

2. Fragments produced by two-photon absorption

a. $C_4H_5^+$

The ion yield of $C_4H_5^+$ exhibits a sharp increase when I increases from $I = 1.1\times10^{13}$ W/cm^2 to 1.7×10^{13} W/cm^2, resulting in the slope of $\beta \sim 6$, implying that $C_4H_5^+$ is generated through multiphoton absorption. However, when $I \leq 1.7\times10^{13}$ W/cm^2, the ion yields of $C_4H_5^+$ are fitted well by a straight line with $\beta = 1.19(14)$. This behavior can be explained by assuming that $C_4H_5^+$ is generated through the $D_4\ E_u$ state by two photon absorption from the $D_0\ E_g$ state, and that $C_6H_{12}^+$ in the $D_4\ E_u$ state is further excited to the $D_5\ E_g$ state by absorbing another photon, from which the smaller fragment ions than $C_4H_5^+$ are created as schematically shown in Fig. 2-5. In this four-state model, when I is higher than a certain critical intensity (I_c), the depletion rate of the $D_4\ E_u$ state by the one-photon transition to the $D_5\ E_g$ state can be almost the same as the creation rate of the D_4 state by the vibronically-allowed two-photon absorption from the $D_0\ E_g$ state via the $D_2\ E_u$ state. By applying the steady state approximation to the $D_4\ E_u$ state, it can be shown that the population of the $D_4\ E_u$ state increases almost linearly to the laser field intensity when $I \geq I_c$, that is, the intensity dependence of the population of the D_4 state changes from I^2 to I^1. Provided $I_c = 1.7\times10^{13}$ W/cm^2, the four-state model is consistent with the observation that the ion yields of $C_4H_5^+$ are fitted well by the straight line whose slope is $\beta = 1.19(14)$ at the higher intensity range of $I \geq 1.7\times10^{13}$ W/cm^2. On the other hand, in the present four-state model, the β value is expected to be ~2 in the lower intensity range of $I \leq 1.7\times10^{13}$ W/cm^2, which seems inconsistent with the experimental β value, $\beta \sim 6$, determined from the data points at $I = 1.1\times10^{13}$ W/cm^2 and $I = 1.7\times10^{13}$ W/cm^2. However, because only four ion counts were recorded for the ion signals of $C_4H_5^+$ at $I = 1.1\times10^{13}$ W/cm^2, it is difficult to discuss the differences in the slope quantitatively.

b. $C_3H_5^+$

The ion yields of $C_3H_5^+$ shown in Fig. 2-6(d) could not be fitted well by a single straight line. The appearance intensity for $C_3H_5^+$ was 2.8×10^{12} W/cm^2, and the β value determined by the ion yields in the lower intensity range of $2.8\times10^{12} \leq I \leq 1.7\times10^{13}$ W/cm^2 is $\beta = 2.21(9)$, while $\beta = 1.11(3)$ is obtained by the ion yields in the higher intensity range of $1.7\times10^{13} \leq I \leq 8.0\times10^{13}$ W/cm^2. Because $\beta \sim 2$ in

the lower intensity range and $\beta \sim 1$ in the higher intensity range, the behavior of the ion yields of $C_3H_5^+$ can be explained well by the four-state model with the threshold laser field intensity, $I_c = 1.7 \times 10^{13}$ W/cm^2, showing that that $C_3H_5^+$ is produced from the D_4 E_u state of $C_6H_{12}^+$.

c. $C_3H_4^+$

The ion yields of $C_3H_4^+$ shown in Fig. 2-6(d) show $\beta \sim 5$ in the lower intensity range of $1.1 \times 10^{13} \leq I$ $\leq 1.7 \times 10^{13}$ W/cm^2 and $\beta = 1.09(11)$ in the higher intensity range of $1.7 \times 10^{13} \leq I \leq 8.0 \times 10^{13}$ W/cm^2. The behavior of $\beta \sim 1$ in the higher intensity range implies that $C_3H_4^+$ is produced from the D_4 E_u state of $C_6H_{12}^+$ on the basis of the four-state model with $I_c = 1.7 \times 10^{13}$ W/cm^2. However, $\beta \sim 5$ determined from the ion yields in the lower intensity range of $1.1 \times 10^{13} \leq I \leq 1.7 \times 10^{13}$ W/cm^2 seems inconsistent with $\beta \sim 2$ expected from the four-state model. Similar to the case in $C_4H_5^+$, the discussion on this inconsistency is difficult because the single data point whose signal count is only ten is available in the intensity range of $I < 1.7 \times 10^{13}$ W/cm^2.

d. $C_2H_4^+$

The ion yields of $C_2H_4^+$ in Fig. 2-6(e) can be fitted with a single slope. The obtained β value is 1.58(5), implying that $C_2H_4^+$ is generated from both of the D_4 E_u state and the D_5 E_g state of $C_6H_{12}^+$ via two photon absorption and three photon absorption, respectively.

3. Fragments produced by three-photon absorption

a. $C_3H_3^+$

The ion yields for $C_3H_3^+$ show a steep slope with $\beta \sim 4$ in the lower intensity range of $1.1 \times 10^{13} \leq I \leq$ 1.7×10^{13} W/cm^2 and $\beta = 1.92(9)$ in the higher intensity range of $1.7 \times 10^{13} \leq I \leq 8.0 \times 10^{13}$ W/cm^2 as shown in Fig. 2-6(d). According to the four-state model, the population of the D_5 E_g state should be proportional to I^3 and I^2 in the intensity regions of $I \leq I_c$ and $I \geq I_c$, respectively. Because the obtained β value is $\beta \sim 2$ in the higher intensity range, it is highly probable that $C_3H_3^+$ is produced from the D_5 E_g state of $C_6H_{12}^+$ as shown in Fig. 2-5. The observed $\beta \sim 4$ in the lower intensity range is slightly larger than $\beta \sim 3$ expected from the four-state model. Again, the discussion on this inconsistency is difficult because the available data point in the intensity range of $I < 1.7 \times 10^{13}$ W/cm^2 is only one, and the obtained signal count for this data point is only nine.

b. $C_2H_5^+$

All the data points for ion yields of $C_2H_5^+$ shown in Fig. 2-6(e) can be fitted with a single slope, and the obtained β value is 1.96(8). Because the β value is $\beta \sim 2$ in the higher intensity range of 1.7×10^{13} $\leq I \leq 8.0 \times 10^{13}$ W/cm^2, $C_2H_5^+$ seems to be produced mainly from the D_5 E_g state of $C_6H_{12}^+$. In this case, the ion yields at the lower intensity range can also be fitted with $\beta \sim 2$, which is inconsistent with $\beta \sim 3$ expected from the four-state model. Although it is difficult to discuss the slope in the lower intensity range determined using the single data point at $I = 1.1 \times 10^{13}$ W/cm^2 with the signal count of 17, this behavior may be ascribed to an additional contribution from $C_2H_5^+$ ions produced from the D_4

E_u state in the lower intensity range via two-photon absorption from the ground D_0 E_g state of $C_6H_{12}^+$.

c. $C_2H_4^+$

As described above, $C_2H_4^+$ is generated from both of the D_4 E_u state and the D_5 E_g state of $C_6H_{12}^+$ via two-photon absorption and via three-photon absorption, respectively.

d. $C_2H_3^+$

The intensity dependence of the ion yields of $C_2H_3^+$ shows a steep slope with $\beta \sim 6$ in the lower intensity range of $1.1 \times 10^{13} \leq I \leq 1.7 \times 10^{13}$ W/cm^2 and $\beta = 1.71(9)$ in the higher intensity range of $1.7 \times 10^{13} \leq I \leq 8.0 \times 10^{13}$ W/cm^2. Because the observed slope is $\beta \sim 2$ in the higher intensity range, it is probable that $C_2H_3^+$ is produced from the D_5 E_g state of $C_6H_{12}^+$ as shown in Fig. 2-5. The observed $\beta \sim 6$ in the lower intensity range seems inconsistent with $\beta \sim 3$ expected from the four-state model. Again, the discussion on this inconsistency is difficult because the single data point whose signal count is only seven is available in the intensity range of $I < 1.7 \times 10^{13}$ W/cm^2.

B. Number of photons absorbed in the fragmentation processes

As discussed in Sec. 2.3.A, it has been estimated from the analyses of the laser intensity dependences of the yields of the fragment ions plotted in Figs. 2-6(a)-(e) by the four-state model with the common critical intensity of $I_c = 1.7 \times 10^{13}$ W/cm^2 that (i) $C_5H_9^+$, $C_4H_n^+$ ($n = 6\sim8$), and $C_3H_n^+$ ($n = 6, 7$) are produced from the D_2 E_u state of $C_6H_{12}^+$ via one-photon absorption, (ii) $C_4H_5^+$, $C_3H_n^+$ ($n = 4, 5$), and $C_2H_4^+$ are produced from the D_4 E_u state of $C_6H_{12}^+$ via two-photon absorption, and (iii) $C_3H_3^+$ and $C_2H_n^+$ ($n = 3\sim5$) are produced from the D_5 E_g state of $C_6H_{12}^+$ via three photon absorption, as schematically summarized in Fig. 2-5. In this section, the excess energies of $C_6H_{12}^+$ generated by the photoabsorption processes estimated above for the respective fragmentation channels are compared with the available literature data of the experimental appearance energies of the respective fragment ions and the experimental heats of formation for the respective decomposition pathways.

In Table I, literature values of the activation energies (E_{AE}) for the production of the respective fragment ions from $C_6H_{12}^+$ in the dissociative ionization of neutral cyclohexane are summarized. These literature values are those obtained by mass spectrometry with the methods of charge-exchange collision [41], electron impact ionization [42-45], and photoionization [46]. The activation energy is defined as $E_{AE} = E_{AP} - E_{IP}$, where E_{AP} is the appearance energy of the fragment ion and E_{IP} is the ionization potential of neutral C_6H_{12}. Therefore, the E_{AE} value can be regarded approximately as the upper bound of the excitation energy of $C_6H_{12}^+$ for the production of the fragment ion. Considering that the photon energy of 800 nm light is 1.55 eV, the E_{AE} values for $C_5H_9^+$, $C_4H_7^+$, $C_4H_8^+$, $C_3H_6^+$ and $C_3H_7^+$, which are lower than or equal to ~1.6 eV (except for the E_{AE} values for $C_3H_6^+$ and $C_3H_7^+$ reported in Ref. [44], indicate that these fragment ions can be produced via one-photon absorption. On the other hand, the E_{AE} values for $C_3H_5^+$ indicate that $C_3H_5^+$ can be produced via two-photon absorption. Therefore, the literature values of E_{AE} are consistent with the numbers of

20

photons absorbed by $C_6H_{12}^+$ estimated by the intensity dependences of the ion yields obtained in the present study.

In the rightmost column of Table I, the thermochemical thresholds (E_{th}) for the dissociation from cyclohexane parent ion $C_6H_{12}^+$ to various fragment ions are listed. These E_{th} values were calculated from the values of heat of formation at 298 K available in the literature [47] for possible combinations of products, and the lowest E_{th} values for the respective product pairs are listed. When the internal energy of $C_6H_{12}^+$ is lower than E_{th}, the corresponding dissociation could not proceed energetically. The E_{th} values for $C_5H_9^+$, $C_4H_n^+$ (n = 6~8), $C_3H_6^+$ and $C_3H_7^+$ are lower than or equal to ~1.6 eV, which are consistent with our estimate that these fragment ion species can be produced via one-photon absorption. The E_{th} values for $C_4H_5^+$, $C_3H_4^+$, $C_3H_5^+$, $C_2H_4^+$, and $C_2H_5^+$, all of which are well above the one-photon energy, 1.55 eV, are also consistent with our estimate based on the laser intensity dependences that these ion species can only be generated by absorption of two or more photons. Furthermore, the E_{th} values for $C_3H_3^+$, 3.53 eV, and that for $C_2H_3^+$, 3.42 eV, are larger than two-photon energy, 3.10 eV, and therefore, $C_3H_3^+$ and $C_2H_3^+$ can be produced by absorbing more than two photons, which is also consistent with our estimate based on the laser intensity dependences that these ion species are produced via three-photon absorption.

2.4. Summary

By the ion-trap mass spectrometry, the decomposition processes of cyclohexane cation $C_6H_{12}^+$ induced by the irradiation of an femtosecond intense laser pulse were investigated. The laser-field intensity dependences of the yields of the fragment ions produced from $C_6H_{12}^+$ were analyzed by the four-state model with the common critical intensity of $I_c = 1.7 \times 10^{13}$ W/cm^2, and the numbers of photons involved in the photoabsorption processes were estimated as follows: (i) $C_5H_9^+$, $C_4H_n^+$ ($n = 6 \sim 8$), and $C_3H_n^+$ ($n = 6, 7$) are produced from the D_2 E_u state of $C_6H_{12}^+$ via one-photon absorption, (ii) $C_4H_5^+$, $C_3H_n^+$ ($n = 4, 5$), and $C_2H_4^+$ are produced from the D_4 E_u state of $C_6H_{12}^+$ via two-photon absorption, and (iii) $C_3H_3^+$ and $C_2H_n^+$ ($n = 3 \sim 5$) are produced from the D_5 E_g state of $C_6H_{12}^+$ via three photon absorption. These photon numbers were consistent with the available data of the experimental appearance energies of the respective fragment ions and with the literature values of the experimental heats of formation for the respective decomposition pathways. The mechanism of the efficient fragmentation processes induced when neutral C_6H_{12} is irradiated with an intense laser pulse was interpreted as the results of the resonant one-photon absorption or that followed by additional absorption of one or two photons in the $C_6H_{12}^+$ cation stage.

Appendix of Chapter 2

In this section, details of the intensity dependences of the yields of fragment ions are explained by the four-state model. Reactions between the electronic ground state D_0, the excited states, D_2, D_4, and D_5 of cyclohexane ions are shown in eq. (A-1), (k_1, k_2, k_3: rate constants for each step),

$$D_0 \xrightarrow{k_1} D_2 \xrightarrow{k_2} D_4 \xrightarrow{k_3} D_5. \tag{A-1}$$

By considering only electronic excitation by laser light, reaction rate equations for each step are shown in eqs. (A-2) - (A-4) (I: laser-field intensity),

$$\frac{d[D_2]}{dt} = k_1 I[D_0] - k_2 I[D_2], \tag{A-2}$$

$$\frac{d[D_4]}{dt} = k_2 I[D_2] - k_3 I[D_4], \tag{A-3}$$

$$\frac{d[D_5]}{dt} = k_3 I[D_4]. \tag{A-4}$$

We use the following assumptions for time $t = 0$,

$$[D_2]_0 = [D_4]_0 = [D_5]_0 = 0, \tag{A-5}$$
$$[D_0]_0 = \text{constant}, \tag{A-6}$$

and the rate constants of the electronically allowed excitation are assumed to be larger than that of the electronically forbidden excitation,

$$k_1, k_3 > k_2. \tag{A-7}$$

At low laser-field intensities, the densities of each state satisfy the following relationship,
$$[D_0] \gg [D_2] \gg [D_4] \gg [D_5]. \tag{A-8}$$

Under this condition, the rate equations can be written as eqs. (A-9) – (A-11),

$$\frac{d[D_2]}{dt} \cong k_1 I[D_0] \propto I, \tag{A-9}$$

$$\frac{d[D_4]}{dt} \cong k_2 I[D_2], \tag{A-10}$$

$$\frac{d[\text{D}_5]}{dt} = k_3 I[\text{D}_4].\tag{A-11}$$

By solving these equations, the densities of each state are obtained as follows,

$$[\text{D}_2] = k_1 It[\text{D}_0] \propto I,\tag{A-12}$$
$$[\text{D}_4] = k_2 It[\text{D}_2] = k_1 k_2 I^2 t^2 [\text{D}_0] \propto I^2,\tag{A-13}$$
$$[\text{D}_5] = k_3 It[\text{D}_4] = k_1 k_2 k_3 I^3 t^3 [\text{D}_0] \propto I^3,\tag{A-14}$$

Showing that the densities of the D_2, D_4, and D_5 states are proportioned to I, I^2, and I^3, respectively. Therefore, the yields of fragments generated from the D_2, D_4, and D_5 states have laser-field intensity dependences of I, I^2, and I^3, respectively.

On the other hand, at laser-field intensities higher than the critical intensity I_c, the reaction rate of the electronically allowed excitation of the D_4 state becomes almost the same as the generation rate of the D_4 state by the vibronically allowed excitation. Then the density of the D_4 state becomes constant (steady-state approximation). Under this condition, the rate equations can be written as,

$$\frac{d[\text{D}_2]}{dt} = k_1 I[\text{D}_0] - k_2 I[\text{D}_2],\tag{A-15}$$

$$\frac{d[\text{D}_4]}{dt} = k_2 I[\text{D}_2] - k_3 I[\text{D}_4] \cong 0,\tag{A-16}$$

$$\frac{d[\text{D}_5]}{dt} = k_3 I[\text{D}_4].\tag{A-17}$$

By solving these equations, the densities of each excited state are obtained as follows,

$$[\text{D}_2] = k_1 It[\text{D}_0] \propto I,\tag{A-18}$$

$$[\text{D}_4] = \frac{k_2}{k_3}[\text{D}_2] = \frac{k_1 k_2 It}{k_3}[\text{D}_0] \propto I,\tag{A-19}$$

$$[\text{D}_5] = k_3 It[\text{D}_4] = k_1 k_2 I^2 t^2 [\text{D}_0] \propto I^2.\tag{A-20}$$

Therefore in laser intensities higher than I_c, laser-field intensity dependences of fragments generated from the D_4 and D_5 states should change to I and I_2.

Chapter 3. Development of an ion beam apparatus

3.1. Introduction

In Chapter 2, the ion trap method in which ions having specific masses are trapped has been developed for investigating dissociation processes of mass-selected ion species in an intense laser field.   There is another method called a high energy molecular ion beam method, with which the dynamics of molecular ions in an intense laser field can also be investigated.

Williams *et al*. [48] measured photodissociation of an H_2^+ ion beam and reported the energy distributions of the fragment species.   They extracted ions generated in a plasma discharge ion source as an ion beam accelerated to the kinetic energy of 1 keV.   The ion beam was momentum-selected by a magnetic sector, and the resultant H_2^+ ion beam with the diameter of 1 mmϕ (FWHM: full-width of half-maximum) was irradiated with ultrashort near-infrared (65 fs, 790 nm, 10 Hz) laser pulses ($\leq 5 \times 10^{15}$ W/cm^2).   The neutral fragments were detected by a detector whereas the fragment H^+ ions were separated from the neutral fragments by an electrostatic deflector and introduced into another detector.   The released kinetic energies of the fragments were recorded at many different laser-field intensities.

On the other hand, Sändig *et al.* [49] investigated the photodissociation processes of H_2^+ by using an H_2^+ ion beam, and reported the two-dimensional momentum projection map of neutral H fragments, which were converted into the 3D momentum distribution of the photofragments.   They extracted ions generated in a dc discharge ion source as 11.1 keV ion beam, and the ion beam was mass-selected by a magnetic sector.   The resultant 50 μm H_2^+ ion beam was irradiated with ultrashort near-infrared ($\geq$ 135 fs, 785 nm, 1 kHz) laser pulses ($\leq 1.5 \times 10^{14}$ W/cm^2).   The parent ions and fragment ions were deflected by an electric fields, and only neutral H fragments were projected onto a MCP detector equipped with a CCD camera.   From the recorded patterns, they obtained 2D momentum projections of the neutral H fragments.   Furthermore, by using laser whose beam axis is perpendicular to the flight axis, the 2D momentum projection was converted into the 3D momentum distribution of the photofragments.

In these ion beam measurements, the repetition rate of measurements could become high enough so that the detection can be synchronized with laser pulses. In addition, neutral fragments can be detectable because their high kinetic energies are sufficiently large along the flight axis.   However, in the earlier studies [48, 49], the obtained information were the kinetic energies of fragment species or the 3D momentum distribution of photofragments from the 2D momentum projection of neutral fragments without coincidence detection of the counter ions.   The coincidence measurements of full 3D momentum of both neutral and ionic fragments required different experimental setup.

The fragmentation processes of molecules in an intense laser field have been investigated by the coincidence momentum imaging (CMI) technique [50]. In this technique, a single neutral molecule is ionized by the irradiation of an intense laser pulse, and then, all the generated fragment ion species accelerated by an electric field are simultaneously detected by a time-and-position sensitive detector. From their flight time and detected position, the 3D momenta of all the fragment ion species can be obtained for the respective ionization events. From the accumulated data set carrying the information of the 3D momenta of the fragment ions, the complete kinematic analyses can be performed for the respective fragmentation pathways. However, as long as only charged fragment ions are detected, this method could not be applied to the investigation of decomposition processes in which one or more neutral fragment species are produced. Ben-Itzhak and coworkers [12, 51, 52] combined the CMI method with a high-energy (5 keV) molecular ion beam source. As an ion source, they used an electron cyclotron resonance ion source with a magnetic sector mass-filter, and investigated dissociation dynamics of small molecular ions containing two or three atoms. In this technique, not only fragment ion species but also neutral fragment species can be detected because the neutral fragments also have sufficiently high kinetic energies to be detected by a MCP detector.

In the present chapter, an ion beam apparatus designed and constructed in our laboratory for the CMI measurements of decomposition processes of polyatomic molecular ions in an intense laser field is introduced and its performance was examined by generating a mass-selected CO_2^+ ion beam. For generating larger sized molecular ions, a duoplasmatron ion source with a collision cell was adopted as an ion source, and for the mass selection, a quadrupole mass-filter having a sufficiently high mass-resolution was introduced.

3.2. Mass-selective ion beam source apparatus

The mass-selective ion beam source apparatus is schematically shown in Fig. 3-1.   In the duoplasmatron ion source (model PS-100 HIS, Peabody Scientific, USA), a neutral Ar gas is ionized to Ar^+ by electric discharge from a Pt mesh filament cathode coated with Ba-Sr-Ca oxides (T-33C-118, Transene Company, Inc., USA), and gaseous CO_2 molecules are ionized by collisional charge transfer from the Ar^+ ions.   The generated ions are extracted by an electric field, and accelerated to 3 keV. The extracted ion beam is mass-selected by the quadrupole mass-filter, and the resultant mass-selected ion beam is separated from background gases by being deflected by the quadrupole deflector.   Then, the resultant continuous-wave (CW) ion beam is chopped into a pulsed ion beam by chopping electrodes, to which pulsed high voltages are applied.   Next, the pulsed ion beam is introduced into the twelve disk electrodes.   The first and the last electrodes are grounded and a high voltage is applied to the central electrode.   The neighboring electrodes are connected by a resister.   When the pulsed ion beam passes through the stack of these electrodes, it is decelerated at the beginning, and is irradiated with a femtosecond laser pulse.   The generated fragment ion species are then reaccelerated at the latter part of the electrodes.   All the fragment species including neutral fragments are detected in coincidence by a time and position sensitive detector with delay line anodes, and the 3D momenta of all the fragment species are obtained from the flight time and detected positions of the species. The parent ion beam is blocked by a movable Faraday cup connected with a XY stage, and its beam current is detected by this Faraday cup.   The detected ion current is measured by an analogue $\mu\mu$A-meter (model MA-10, Horiba, Ltd. JPN).

Quadrupole deflector
→ Separation of ion beam from background gases

Chopping electrode
→ Formation of pulsed ion beam

Quadrupole mass filter
→ Mass selection of ion beam

Fragment species

3 keV ion beam

5 kHz laser pulses

Twelve disk electrodes
→ Deceleration of ion beam and acceleration of fragment ions for CMI

Movable Faraday cup
→ Measurement of parent ion beam currents

Duoplasmatron ion source with a collision cell
→ Molecular ion generation by collisional charge transfer

$$Ar + e^- \rightarrow Ar^+ + 2e^-$$
$$CO_2 + Ar^+ \rightarrow CO_2^+ + Ar$$

Time and position sensitive detector with delay-lines
→ Measurement of 3D momenta of all the fragment species

Fig. 3-1. Schematics of the mass-selective ion beam apparatus for CMI measurements.

A. Quadrupole mass filter

In this section, the theory of a quadrupole mass filter is explained [53]. A quadrupole mass filter is a device with which charged particles are selected by their mass-to-charge ratio (*m/z*). A quadrupole electric field is generated by applying dc and ac voltages to four parallel rod electrodes, and charged particles flying along the central axis of the electrodes are selected by their *m/z*.

A voltage Φ, which is the sum of the dc voltage U and the ac voltage $V\cos\Omega t$ defined as

$$\Phi = -U + V\cos\Omega t, \qquad\qquad (3\text{-}1)$$

where t denotes time and Ω denotes the angular frequency, is applied onto the four rod electrodes so that the coordinates X and Y in the cross section shown in Fig. 3-2 satisfy the relation of $X^2 - Y^2 = R_0^2$, where $2R_0$ represents the shortest distance of the opposite electrodes.

When a charged particle with the mass-to-charge ratio *m/z* flies along the direction perpendicular to the central axis, the equations of motions of this particle are written as

$$m\frac{d^2X}{dt^2} = -\frac{2ze}{R_0^2}(-U + V\cos\Omega t)X, \qquad\qquad (3\text{-}1)$$

$$m\frac{d^2Y}{dt^2} = +\frac{2ze}{R_0^2}(-U + V\cos\Omega t)Y. \qquad\qquad (3\text{-}2)$$

These two equations can be converted into the Mathieu equation,

$$\frac{d^2u}{d\tau^2} + (a - 2q\cos2\tau)u = 0, \qquad\qquad (3\text{-}3)$$

where u represents

$$u = X, Y, \qquad\qquad (3\text{-}4)$$

and τ, a, and q are given as

$$\tau = \frac{\Omega t}{2}, \qquad\qquad (3\text{-}5)$$

$$a = a_Y = -a_X = \frac{8zeU}{m\Omega^2 R_0^2}, \qquad\qquad (3\text{-}6)$$

29

$$q = q_Y = -q_X = \frac{4zeV}{m\Omega^2 R_0^2}.$$
(3-7)

Whether a stable solution of this Mathieu equation exists depends on the two parameters a and q. When the parameters a and q are in the stability zones on the $a-q$ plane, a charged particle can pass through the mass filter.   In Fig. 3-3, the first stability zones for the two different m/z values are shown on the $U-V$ plane.   By varying the voltages while keeping the U/V ratio constant along the scan line, the m/z value of the particle that can pass through the mass filter is varied, and consequently, the mass selection can be achieved depending on the m/z value.   The resolving power of the mass filter depends on the slope of the scan line, and can be maximized when the line is on the peak of the stability zone ($a = 0.237$, $q = 0.706$).

Ideally, the cross section of the rod electrodes should have the hyperbolical shape as shown in Fig. 3.2.   However, because this shape is difficult to be manufactured, cylindrical rods whose cross section is round shaped are used in most cases.   In order to make the electric field generated using the cylindrical electrodes as close as possible to a pure quadrupole field, the intervals of $2R_0$ are adjusted.   When the ratio R/R_0 is ~1.127, where R denotes the radius of the circular rods, the impurities of the higher order multipole terms in the electric fields becomes smallest [54].   In the design of the quadrupole mass filter adopted in this thesis study, this ratio of $R/R_0 = 1.127$ was also adopted.
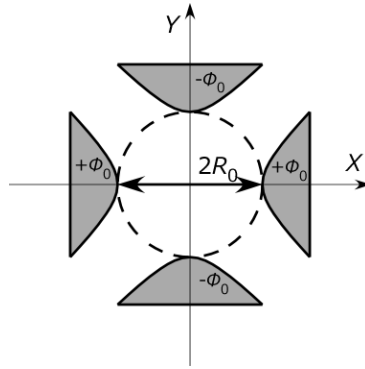
Fig. 3.2. An ideal cross section of the four rods of a quadrupole mass filter.
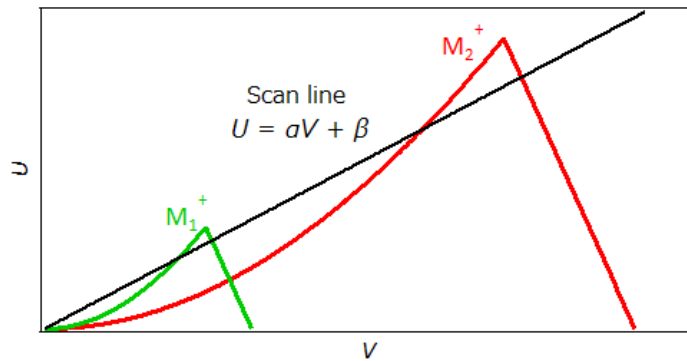
Fig. 3-3. First stability zones for the different masses in the quadrupole mass filter.

B. The components of the ion beam apparatus

The ion source adopted in the thesis study is a duoplasmatron ion source, in which ions are generated by electric discharge.　In the ion source, a filament cathode is heated to emit thermal electrons from its surface, and the accelerated electrons collide with gaseous atoms and/or molecules and ionize them during their flight toward the anode.　The secondary electrons generated through the collisional processes are accelerated by the electric field and collide with other gaseous atoms and/or molecules, inducing further ionization.　The gas that the accelerated electrons collide is called a "carrier gas". In this study, I adopted an Ar gas as the carrier gas.　For generation of ion species which could not be made from the carrier gas, gaseous sample atoms/molecules are introduced into the duoplasmatron ion source together with the carrier gas so that these ions are produced via the collision with the carrier gas ions through the charge transfer ionization processes.　The generated ions and electrons are stored as a plasma in the ion source by a magnetic field generated by the electromagnets.　The generated plasma is compressed magnetically around the anode by the magnetic field so that it could go out through a small hole on the anode.
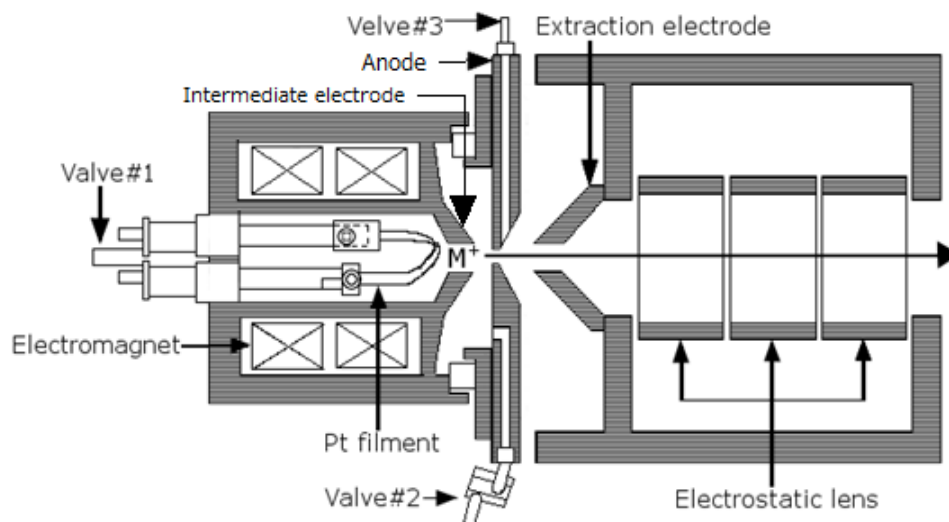
Fig. 3-4. The Model PS-100HIS (Peabody Scientific, Co.) duoplasmatron ion source (taken from the operation manual of Model PS-100HIS).

The duoplasmatron ion source used in the present study, shown in Fig. 3-4 and Fig. 3-5 (b), is Model PS-100HIS (Peabody Scientific) equipped with three valves through which the carrier gas and sample gases are introduced.　The Valve #3 is placed slightly away from the filament cathode so that the cathode becomes free from the damage to be induced by highly reactive gases like O_2.　For the generation of positive ions, a carrier gas is introduced from the Valve#2 and a target sample gas is introduced from the Valve#3.　For the generation of negative ions, a carrier gas is introduced from the Valve#1 and a target sample gas is introduced from the Valve#2.　A negative ion beam can also be generated without using a charge exchange cell by moving slightly the axis of the intermediate electrode respect to the axis of the anode aperture. The optimum offset is about 1 mm for this ion source.

The Pt mesh filament cathode (Fig. 3-5 (c)) is coated with Ba-Sr-Ca oxides so that it can emit thermal electrons efficiently.　In the duoplasmatron ion source (model PS-100 HIS, Peabody Scientific, USA), a neutral Ar gas is ionized to Ar^+ by electric discharge from a Pt mesh cathode coated with Ba-Sr-Ca carbonate (T-33C-118, Transene Company, Inc., USA), and gaseous CO_2 molecules are ionized by collisional charge transfer from the Ar^+ ions.

For the coating with the oxidation, a Pt mesh filament was first cleaned by the etching in diluted nitric acid followed by the rinsing with distilled water, and then, the Pt mesh was dipped into a solution of a coating material (Ba-Sr-Ca: 56-31-13%) so that it is coated with carbonates.　Finally, the Pt mesh coated with carbonates was activated by the heating up to about 1200 °C under the vacuum conditions (below 1×10^{-3} Pa), through which the carbonate is converted into oxides as

$$(Ba/Sr/Ca)CO_3 \xrightarrow{\text{heat}} (Ba/Sr/Ca)O + CO_2 \uparrow. \qquad (3\text{-}8)$$
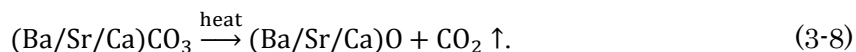
In the ion source, the high voltage (3 kV) is applied to the Pt mesh filament cathode so that

the cascade formation of the plasma proceeds, and the generated ion species are extracted through a hole on the grounded anode.　The extracted ion beam with the average kinetic energy of 3 keV is collimated and decelerated to about 20 eV by an electrostatic lens, and is introduced into a mass filter. The electrostatic lens is composed of three tube electrodes: a grounded entrance electrode, a central electrode (2980±40 V), and an exit electrode (2980 V).　Through the optimization of the voltage applied to the central electrode, the ion beam is focused on the entrance of the mass filter and is introduced into it with a high efficiency.

　　　　The quadrupole mass filter (Fig. 3-5 (d)) is composed of four main rod electrodes, four pre-filter rod electrodes, and four post-filter rod electrodes.　The four main rod electrodes are aluminum alloy cylindrical rod whose diameter and length are 20 mm and 300 mm, respectively.　The diameter of all the cylindrical rods in the pre-filter and the post-filter is 20 mm and its length is 20 mm.　To the main rod electrodes, both DC voltage and AC (~1.2 MHz) voltage are applied, while to the electrodes in the pre-filter and the post-filter, only AC voltage is applied.　By the electric fields generated by the pre-filter and the post-filter, the distortion in the fringing fields appearing on both sides of the four main rod electrodes is reduced.　The voltage applied to the housing in which the mass filter is installed was set to be 2980 V, and the ion beam passing through the mass filter has a kinetic energy of ~20 eV.　The AC voltage in the radio-frequency range was generated by a handmade circuit whose design was taken from Ref. 55.

　　　　During the mass selection, the ion beam is shaken by AC voltages in the mass filter, and the divergence of the ion beam after it passes the mass filter is adjusted by the electrostatic lens.　This lens is composed of nine disk electrodes with the 0.3 mm thickness and the inner hole diameter of 20 mmϕ stacked with 8 mm intervals.　The different voltages are applied to the nine stacked electrodes. The last disk electrode on the exit side is grounded so that the ion beam can be reaccelerated to 3 keV.

　　　　The reaccelerated ion beam is introduced into the quadrupole deflector (Fig. 3-5 (e)) and separated by the deflection from background gases and neutralized ions.　This deflector is composed of four quartered cylindrical rod electrodes whose radius and the length are 20 mm and 40 mm, respectively.　For the ion beam deflection, the voltage of about +2.5 eV is applied to a pair of the electrodes facing opposite to each other with respect to the central axis and the voltage of about −2.5 kV is applied to another pair of the electrodes.　The deflected ion beam passes through an aperture with the 1 mm diameter to be introduced into the next collimation stage.

　　　　The ion beam is then collimated by an electrostatic lens composed of three cylindrical electrodes with the 12 mm inner diameter and 12 mm length.　The entrance and exit electrodes are grounded, and the voltage (~2 kV) applied to the central electrode is varied for the optimization of the ion current.

　　　　The velocities of the collimated ion beam perpendicular to the flight axis are adjusted by two set of plate deflectors.　These two deflectors are composed of a pair of plate electrodes with the

33

18 mm length (along the ion beam propagation direction) and 46 mm width (along the direction perpendicular to the ion beam propagation direction).   The spatial gap between the facing electrode plates is 8 mm for both of the deflectors.   The plus and minus voltages applied to each electrode are varied in the range between 0 and −40 V and between 0 and +40 V so that their magnitudes are the same.

After passing the plate deflectors, the ion beam is chopped into a pulsed beam by the chopping electrodes composed of a pair of plate with the 5 mm length and 30 mm width whose spatial gap is set to be 4 mm.   Pulsed high voltages (up to ±950 V) are applied to the chopping electrodes from a pulsed voltage generator (PVM-4210, Directed Energy, Inc., USA) controlled by a delay generator, model DG535 (Stanford Research Systems, Inc., USA).

Finally, the pulsed ion beam is introduced into a set of twelve stacked disk electrodes (Fig. 3-5 (f)).   The width of all the twelve disk electrode is 1 mm and their intervals are set to be 4 mm. The inner diameter of the first disk is 1 mm and that of the fifth central disk is 2 mm while the diameters of the other ten disks are all 30 mm.   A set of stacked electrodes having a similar function to the one introduced in the present study can be found in Ref. 17.

For the final 4mm thick disk electrodes, a 12 mm cylinder with 30 mm inner diameter and 32 mm outer diameter is welded for reduction of effects from outer fields.   The first and the last electrodes are grounded, and a high voltage of ~+1.6 kV is applied to the fifth central electrode.   The neighboring electrodes are connected by a resister having the resistance of 3.3 MΩ.   The introduced ion beam is decelerated until the central fifth electrode, and then, interacts with an intense laser pulse between the fifth and the sixth electrodes.   The parent ion beam and generated ions are reaccelerated by the latter half of the stacked electrodes.   The reaccelerated fragment ions and non-accelerated neutral fragments are projected onto a MCP detector to be detected.   The parent ion beam is blocked by a movable Faraday cup (Fig. 3-5 (g)), which is composed of a hollow cylinder with the 3 mm inner diameter, in front of the MCP detector.   The charges of the blocked ion beam are recorded as an electric current by the μμA meter (model MA-10, Horiba, Ltd., JPN).

When the 2D projection pattern of the parent ion beam is recorded, the Faraday cup is moved out from the flight axis of the ion beam, and the ion signals are detected by a MCP detector equipped with a phosphor screen   (Fig. 3-5 (h)) coupled with a CCD camera (model DV434, Andor Technology, Ltd., GBR).   The fluorescence images recorded by the CCD camera are analyzed by a personal computer.   When the coincidence measurements of the fragment species are performed, the ion beam is blocked by the Faraday cup, and fragments are detected by a MCP detector equipped with delay line anodes, and 3D momentum distributions of the fragments are obtained by accumulating coincidence events.
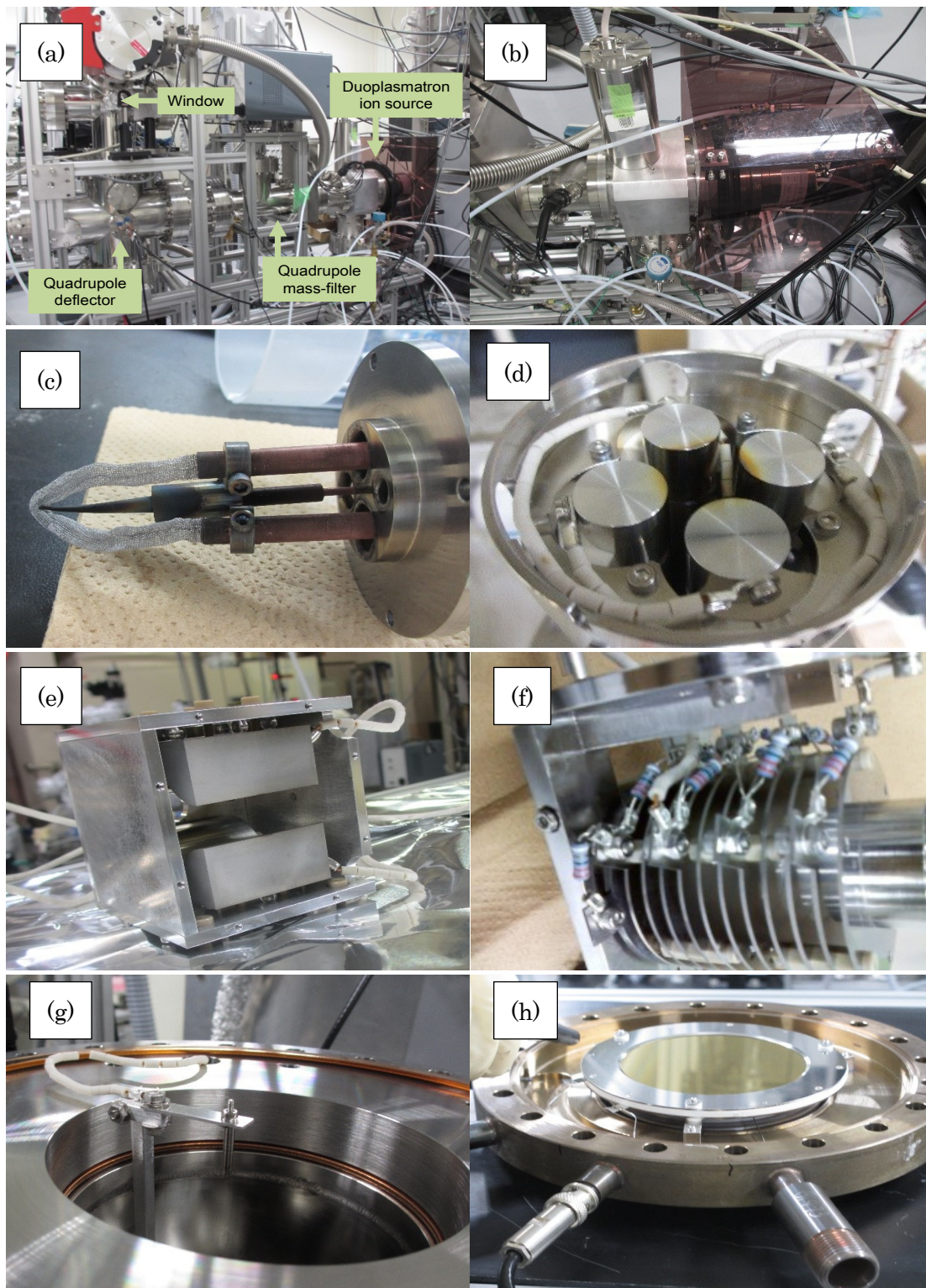
Fig. 3-5. Photographs of the constructed ion beam source. (a) Overview of the apparatus, (b) the duoplasmatron ion source, (c) Pt filament, (d) the quadrupole mass filter, (e) the quadrupole deflector, (f) the twelve stacked disk electrodes, (g) the movable Faraday cup, and (h) the MCP detector with phosphor screen.

3.3. Mass-selected CO_2^+ ion beam generation

First, a mass-selective CO_2^+ ion beam was generated by the duoplasmatron ion source.　A carrier Ar gas was introduced from the Valve#2, and a target gas, CO_2 gas, was introduced from the Valve#3 for the generation of CO_2^+ ion.　The voltage of –150 V was applied to the Pt mesh filament, which is heated by a 30 A electric current for the electric discharge.　The generated ions, stored as a plasma by the magnetic field generated by the electromagnets, was extracted from the ion source.　The extracted ion beam, in which no only CO_2^+ ions but also Ar^+ ions and the other impurity ions are included, was introduced into the mass filter for the mass selection.　In this section, the conditions under which CO_2^+ ions ($m/z = 44$) are separated completely from Ar^+ ions ($m/z = 40$) is explored so that a sufficiently high ion current is achieved for CO_2^+ ions.

　　　　By a careful optimization of the voltages applied to the electrodes of the quadrupole mass filter, a mass spectrum of the generated ion beam passing through the mass filter was obtained as shown in Fig. 3-6, in which the yield of CO_2^+ ions is much larger than the yield of Ar^+ ions.　From this spectra, the mass-resolution ($m/\Delta m$) of the mass-filter was estimated to be about 48 when the ion beam current of CO_2^+ was about 150 pA.
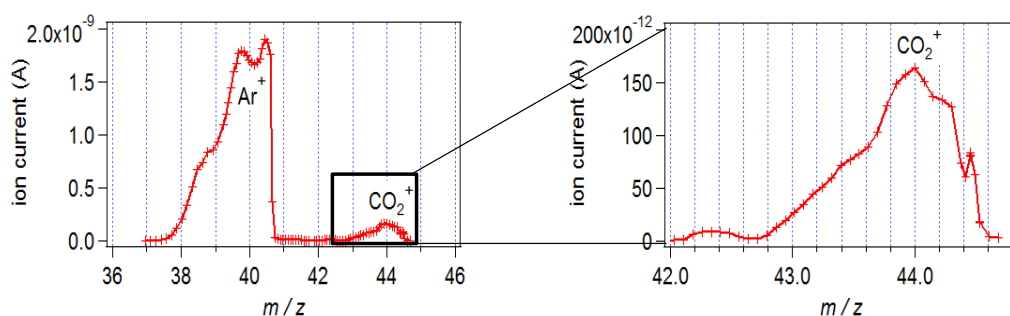
Fig. 3-6. Mass spectra of the generated ion beam after it passed through the quadrupole mass filter in the m/z range between 36 and 46 (left) and in the region near $m/z = 44$ (right). The horizontal axis represents the mass-to-charge ratio converted using the applied voltages.　The vertical axis represents the ion current measured by the Faraday cup.

36

3.4. Characteristics of CO_2^+ ion beam

The generated continuous CO_2^+ ion beam was converted into a pulsed ion beam by applying the pulsed high voltages (1 kHz, 1 μsec, and ±950 V) to the chopping electrodes.   The Faraday cup was moved out from the flight axis, and the pulsed ion beam was projected onto the MCP phosphor imaging detector.   The fluorescence image on the phosphor screen was captured by a CCD camera with the exposure time of 0.1 sec, and was recorded by a personal computer.

When the continuous CO_2^+ ion beam current is 300 pA, the beam profile shown in Fig. 3-7 was obtained.   The FWHMs of the oval shaped ion beam profile were found to be about 2.1 mm for the major axis and about 1.7 mm for the minor axis.   From the beam profile and the beam current, the ion density was calculated to be about 6×10^3 cm^{-3}.   By assuming that 1% of parent CO_2^+ ions dissociate by the irradiation of 5 kHz laser pulses whose diameter is 100 μm, the count rate of the fragment signals was estimated to be about 2 cps (0.04 counts/shot).   By the comparison with the detection conditions achieved in our previous coincidence experiments [56], this estimated count rate is expected to be sufficiently large for coincidence measurements of fragmentation processes of CO_2^+.

FWHM ~ 2.1 mm

FWHM ~ 1.7 mm
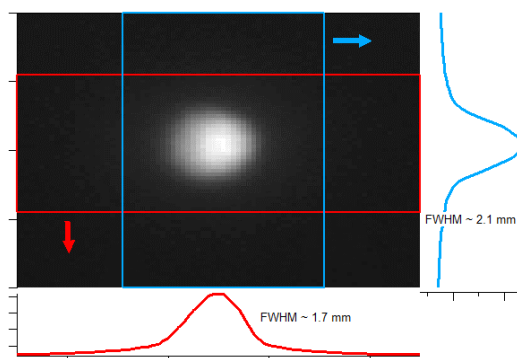
Fig. 3-7. A beam profile of the CO_2^+ ion beam measured by a MCP/Phosphor imaging detector equipped with a CCD camera.   The ion beam current is ~300 pA.

3.5. Summary

A mass-selected ion beam apparatus composed of the duoplasmatron ion source and the quadrupole mass filter was developed, and a sufficiently intense CO_2^+ ion beam was obtained with negligible contamination of Ar^+ ions thanks to the mass resolution of about 48 achieved by the quadrupole mass-filter. It was confirmed that the estimated density of the CO_2^+ ion beam was sufficiently large for coincidence measurements of the fragmentation processes. As a next step in the future, photodissociation processes of CO_2^+ and other molecular ion species will be investigated by combining the CMI technique.

Chapter 4. Summary and future directions

In the present thesis, I developed two different experimental methods, which can be applied for investigating photodecomposition processes of mass selected molecular ion species.

In Chapter 2, in the study on the "decomposition of trapped cyclohexane parent ions in intense laser fields", I observed the decomposition of cyclohexane parent ions induced by intense ultrafast laser pulses by the method of ion-trap time-of-flight mass spectrometry. Many kinds of photofragment ion species were identified in the mass spectra as the result of the decomposition of mass-selectively trapped cyclohexane parent ions, indicating that the decomposition of parent $C_6H_{12}^+$ ions proceeds efficiently by the photo-irradiation of 800 nm. From the laser-fields intensity dependences of the yields of fragment ions, the numbers of absorbed photons for producing the respective fragment ions are estimated, and the fragment ions were categorized into three groups by the four state model. The resultant photon numbers were consisted with the literature values of the experimental appearance energies of the respective fragment ions as well as with the heats of formations for the respective decomposition pathways. The mechanism of the excessive fragmentation processes of neutral cyclohexane by the irradiation of intense 800 nm laser pulses was interpreted as the results of the fragmentation processes in the parent cyclohexane cation stage in which the fragmentation proceeds after the one-photon resonance absorption and/or after the one-photon resonance absorption followed by additional one-photon or two-photon absorption processes.

In Chapter 3, in the study on the "development of an ion beam apparatus", I developed the mass selective ion beam apparatus designed for the coincidence measurements of fragment species generated from intense-fields photodecomposition processes of mass selected molecular ion species. The ion beam extracted from the duoplasmatron ion source was mass selected after it passed through the quadrupole mass filter, and it was confirmed that a CO_2^+ ion beam with sufficiently high purity was generated with the ion current of about 150 pA. From the obtained beam profile of the CO_2^+ ion beam, the FWHM values of the beam were determined to be 2.1 mm and 1.7 mm for the major axis and the minor axis, respectively. From the obtained data, the signal count rate for the intense field photodecomposition of CO_2^+ was estimated to be about 2 count per seconds under the assumption of that 1% of the parent ions are decomposed when they are irradiated with a 5 kHz laser pulse having the spatial diameter (FWHM) of 100 μm. The estimated count rate is sufficiently large for the coincidence measurements of the fragment to be generated from CO_2^+.

Both of the two methods I introduced in the present thesis are considered to be efficient as well as promising for investigating photoinduced decompotision processes of a variety mass selected ion species. It is expected that interaction between mass selected ion species with ultrashort intense laser pulses will be more extensively investigated in the near future by taking advantage of the ion-trap mass spectrometry and the ion beam mass spectrometry whose applicability has been examined and explored here.

Acknowledgements

References

[1] A. Assion, T. Baumert, U. Wiechmann, and G. Gerber, Phys. Rev. Lett. **86**, 5695 (2001).

[2] I. Ben-Itzhak, in *Progress in Ultrafast Intense Laser Science IV* (Springer-Verlag Berlin Heidelberg 2009) p. 68.

[3] R. Itakura, J. Watanabe, A. Hishikawa, and K. Yamanouchi, J. Chem. Phys. **114**, 5598 (2001).

[4] J. Watanabe, R. Itakura, A. Hishikawa, and K. Yamanouchi, J. Chem. Phys. **116**, 9697 (2002).

[5] R. Itakura, T. Tanaka, M. Kuwata, H. Suzuki, and K. Yamanouchi, Chem. Phys. Lett. **462**, 27 (2008).

[6] R. Itakura, T. Asano, and K. Yamanouchi, J. Photochem. Photobiol. A **158**, 77 (2003).

[7] R. Itakura, K. Yamanouchi, T. Yasuike, and K. Someda, Chem. Phys. Lett. **396**, 208 (2004).

[8] C. L. Kalcic, T. C. Gunaratne, A. D. Jones, M. Dantus, and G. E. Reid, J. Am. Chem. Soc. **131**, 940 (2009).

[9] S. A. Smith, C. L. Kalcic, K. A. Safran, P. M. Stemmer, M. Dantus, and G. E. Reid, J. Am. Soc. Mass Spectrom. **21**, 2031 (2010).

[10] S. A. Smith, C. L. Kalcic, L. Cui, and G. E. Reid, Rapid Commun. Mass Spectrom. **27**, 2807 (2013).

[11] T. Yamazaki, Y. Watanabe, R. Kanya, and K. Yamanouchi, J. Chem. Phys. **144**, 024313 (2016).

[12] I. Ben-Itzhak. P. Q. Wang. J. F. Xia, A. M. Sayler, M. A. Smith, K. D. Carns, and B. D. Esry, Phys. Rev. Lett. 95, 073002 (2005).

[13] B. Gaire, A. M. Sayler, P. Q. Wang, N. G. Johnson, M. Leonard, E. Parke, K. D. Carnes, and I. Ben-Itzhak, Rev. Sci. Instrum. **78**, 024503 (2007).

[14] N. Takahashi, Y. Adachi, M. Saito, and, Y. Haruyama, Nucl. Instrum. Meth. B, **315**, 51 (2013).

[15] M. J. DeWitt, and R. J. Levis, J. Chem. Phys. **102**, 8670 (1995).

[16] M. J. DeWitt, D. W. Peters, and R. J. Levis, Chem. Phys. **218**, 211 (1997).

[17] D. J. Smith, K. W. D. Ledingham, H. S. Kilic, T. McCanny, W. X. Peng, R. P. Singhal, A. J. Langley, P. F. Taday, and C. Kosmidis, J. Phys. Chem. A **102**, 2519 (1998).

[18] K. W. D. Ledingham, R. P. Singhal, D. J. Smith, T. McCanny, P. Graham, H. S. Kilic, W. X. Peng, S. L. Wang, A. J. Langley, P. F. Taday, and C. Kosmidis, J. Phys. Chem. A **102**, 3002 (1998).

[19] K. W. D. Ledingham, D. J. Smith, T. McCanny, P. Graham, H. S. Kilic, W. X. Peng, A. J. Langley, P. F. Taday, and C. Kosmidis, J. Phys. Chem. A **103**, 2952 (1999).

[20] C. Kosmidis, P. Tzallas, K. W. D. Ledingham, T. McCanny, R. P. Singhal, P. F. Taday, and A. J. Langley, J. Phys. Chem. A **103**, 6950 (1999).

[21] M. J. DeWitt, and R. J. Levis, J. Chem. Phys. **108**, 7045 (1998).

[22] M. Castillejo, S. Couris, E. Koudoumas, and M. Martín, Chem. Phys. Lett. **289**, 303 (1998).

[23] M. Castillejo, S. Couris, E. Koudoumas, and M. Martín, Chem. Phys. Lett. **308**, 373 (1999).

[24] M. J. DeWitt, and R. J. Levis, J. Chem. Phys. **110**, 11368 (1999).

[25] W. Fuß, W. E. Schmid, and S. A. Trushin, J. Chem. Phys. **112**, 8347 (2000).

[26] H. Harada, S. Shimizu, T. Yatsuhashi, S. Sakabe, Y. Izawa, and N. Nakashima, Chem. Phys. Lett. **342**, 563 (2001).

[27] M. Murakami, R. Mizoguchi, Y. Shimada, T. Yatsuhashi, and N. Nakashima, Chem. Phys. Lett. **403**, 238 (2005).

[28] M. Tanaka, S. Panja, M. Murakami, T. Yatsuhashi, and N. Nakashima, Chem. Phys. Lett. **427**, 255 (2006).

[29] M. Tanaka, M. Kawaji, T. Yatsuhashi, and N. Nakashima, J. Phys. Chem. A **113**, 12056 (2009).

[30] K. Kato, and K. Yamanouchi, Chem. Phys. Lett. **397**, 237 (2004).

[31] S. M. Hankin, D. M. Villeneuve, and P. B. Corkum, D. M. Rayner, Phys. Rev. A **64**, 013405 (2001).

[32] K. Hoshina, Y. Furukawa, T. Okino, and K. Yamanouchi, J. Chem. Phys. **129**, 104302 (2008).

[33] H. Wu, S. Zhang, J. Zhang, Y. Yang, L. Deng, T. Jia, Z. Wang, and Z. Sun, J. Phys. Chem. A **119**, 2052 (2015).

[34] T. Shida, and Y. Takemura, Radiat. Phys. Chem. **21**, 157 (1983).

[35] R. Mehnert, O. Brede, and W. Naumann, J. Radioanal. Nucl. Chem. **101**, 307 (1986).

[36] I. A. Shkrob, M. C. Sauer Jr., and A. D. Trifunac, J. Phys. Chem. **100**, 7237 (1996).

[37] W. C. Wiley, and I. H. McLaren, Rev. Sci. Instrum. **26**, 1150 (1955).

[38] S. Guan, and A. G. Marshall, Int. J. Mass Spectrom. Ion Processes **157/158**, 5 (1996).

[39] H. Xu, T. Okino, K. Nakai, and K. Yamanouchi, in *Progress in Ultrafast Intense Laser Science VII* (Springer-Verlag Berlin Heidelberg 2011) p. 35.

[40] S. X. Tian, N. Kishimoto, and K. Ohno, J. Phys. Chem. A **106**, 6541 (2002).

[41] J. A. Herman, Y.-H. Li, and A. G. Harrison, Org. Mass Spectrom. **17**, 143 (1982).

[42] J. P. Puttemans, Ing. Chim. (Brussels) **56**, 64 (1974).

[43] F. P. Lossing, J. C. Traeger, and Int. J. Mass Spectrom. Ion Phys. **19**, 9 (1976).

[44] F. P. Lossing, and J. C. Traeger, J. Am. Chem. Soc. **97**, 1579 (1975).

[45] M. A. Rabbih, E. T. M. Selim, and M. A. Fahmey, Indian J. Pure Appl. Phys. **19**, 962 (1981).

[46] Y. L. Sergeev, M. E. Akopyan, and F. I. Vilesov, Y. V. Chizhov, High Energy Chem. **7**, 369 (1973).

[47] S. G. Lias, J. E. Bartmess, J. F. Liebman, J. L. Holmes, R. D. Levin, and W. G. Mallard, J. Phys. Chem. Ref. Data **17**, Suppl. 1 (1988).

[48] I. D. Williams, P. McKenna, B. Srigengan, I. M. G. Johnston, W. A. Bryan, J. H. Sanderson, A. El-Zein, T. R. J. Goodworth, W. R. Newell, P. F. Taday, and A. J. Langley, J. Phys. B, **33**, 2743 (2000).

[49] K. Sändig, H. Figger, and T. W. Hänsch, Phys. Rev. Lett. **85**, 4876 (2000).

[50] H. Hasegawa, A. Hishikawa, and K. Yamanouchi, Phys. Rev. Lett. **349**, 57 (2001).

[51] I. Ben-Itzhak, P. Wang, J. Xia, A. M. Sayler, M. A. Smith, J. W. Maseberg, K. D. Carnes, and B. D. Esry, Nucl. Instrum. Methods in Phys. Research B, **233**, 56 (2005).

[52] J. McKenna, A. M. Sayler, B. Gaire, Nora G. Johnson, K. D. Carnes, B. D. Esry, and I. Ben-Itzhak, Phys. Rev. Lett. **103**, 103004 (2009)

[53] W. Paul, Rev. Modern. Phys. **62**, 531 (1990).

[54] T. J. Hogan, and S. Taylor, IEEE Trans. Instrum. Meas. **57** 498 (2008).

[55] R. M. Jones and S. L. Anderson, Rev. Sci. Instrum. **7**, 4335 (2000).

[56] R. Kanya, T. Kudou, N. Schirmel, S. Miura, K.-M. Weitzel, K. Hoshina, and K. Yamanouchi, J. Chem. Phys. **136**, 204309 (2012).